Dalton Transactions

Accepted Manuscript

ROYAL SOCIETY OF CHEMISTRY

www.rsc.org/dalton

Template free constructing hollow Fe_3O_4 architecture embedded in N-doped graphene matrix for lithium storage

Guohui Qin[a,b*] , Zewei Fang [ab], Chengyang Wang [a,b,*]

[a] School of Chemical Engineering and Technology, Tianjin University, Tianjin 300072, China

[b] Collaborative Innovation Center of Chemical Science and Engineering, Tianjin 300072, China

Corresponding author. Tel.: +86 22 27890481; fax: +86 22 27890481.

E-mail address: guohuiq163@sina.com, cywang@tju.edu.cn (C. Wang)

Rational design and fabrication the electrode material is of significance and yet great challenging task. In this work, the mesoporous Fe_3O_4 nanostructures featured by 3D structured hollow nanoparticles decorated by N-doped graphene with an average of 10nm were synthesized by a combination of hydrothermal and post carbonization technique, subsequently studied as an anode material for lithium ion batteries.Such hollow nanoarchitecture anchored on N-doped graphene sheets possessing the large specific surface area and enhanced volumetric capacity offers maximum lithium storage, facilitates rapid electrochemical kinetics, buffers volume changes during lithium ion insertion and extraction progress and removes the detrimental active sites due to the N incorporation which is the bottleneck of improving the recycle ability of the anode materials. High reversible capacities, excellent rate-capability and stable performance were continuously observed. Accordingly, the graphene-based composites by intercalating hollow Fe_3O_4 nanocrystals into N-doped graphene sheets have evidenced to be promising electrode materials for energy store.

Introduction

Fabrication rational nanostructures with controllable morphology, composition, and internal architectures is challenging for developing lithium ion batteries (LIBs) with high energy density, power density and cycling stability.[1-4] Hollow-shell metal oxide nanostructures with high surface area, excellent mass transfer properties, and high lithium ion capacity have been considered as an promising anode materials for LIBs.[5-9] In this context, magnetite (Fe_3O_4) has received considerable attention by virtue of its high theoretical capacity (926 mAh g^{-1}),low cost and high natural abundance, and environmentally friendly characteristic.[10,11] Despite its fascinating advantages, the kinetic limitations factors including the drastic volume expansion (>200%) and agglomeration of Fe_3O_4 nanoparticles during the Li^+ insertion/extraction process lead to poor rate capability and low capacity retention arising capacity loss, poor cycling stability severe pulverization of the electrodes accompanying poor conductivity, which seriously restrict its practical application in LIBs.[12-15]

To address these challenges, the strategy combining both integrated electrode design and porous structure with low-dimensional building blocks in electrode configurations has been confirmed to be a potential technique. As to the electrode design, the material composite engineering was successfully evaluated by the integration of Fe_3O_4 particles with various carbon materials for the purpose of improving the electrochemical performance of Fe_3O_4.[16-20] Among these, graphene can serve as a promising matrix to host Fe_3O_4 due to its intrinsic feature of superior electron transport properties, large surface area, outstanding mechanical strength and

excellent chemical stability,[18] which can supply a large electrode/electrolyte contact area, a shortened transport distance and promoted diffusion rates for both lithium ions and electrons.[21] By virtue of such unique design rationales, the electrochemical activity of electrode materials can be greatly improved because of the fast charge transfer and excellent structural integrity.

As to the morphology tailoring technology, nanosized porous Fe_3O_4 crystals with various morphologies, such as nanowires, nanosheets, nanotubes and nanospheres that are expected to buffer the mechanical stresses that could dramatically improve the lithium store performance have been intensively investigated.[22-27]In particular, hollow structures as an unusual morphological class of materials have been identified into the ideal model for a high performance electronic anode material and evoked manifold interest. The hollow nanoscale structure with the abundant interspace voids can not only easily accommodate the mechanical stress caused by the large volume change during Li^+ insertion/extraction but also guarantee ample penetration of electrolyte and fast diffusion of Li^+ ions which are high desirable for improving the accessibility of the host materials to lithium ions. The unique nanostructure can efficiently increase the specific surface area, which can ensure sufficient contact with the electrolyte and active materials. Simultaneously, the free volume in the hollow structure can also shorten the diffusion length of Li^+ ions and lead to superior electrochemical dynamic behavior. It is therefore envisioned that the incorporation of ancillary components and morphology engineering technique can significantly enhance the electrochemical performance of Fe_3O_4 anode materials in

terms of excellent cycling stability and rate capability.

Synchronously, surface modification engineering, for example N doping should be combined for the purpose of solidifying the interface between the graphene and Fe_3O_4.Such modified nanocrystals can offer shortened solid-phase ion diffusion length and excellent conductivity within the particles. Besides the improved ion and electron conductivity, the fabricated architecture also effectively circumvents the issues associated with the a solid electrolyte interface (SEI) formation which leads to irreversible capacity loss. Therefore, the Fe_3O_4 nanomaterials used in LIBs usually suffer from large irreversible capacity due to formation of SEI layer. Generally, the Fe_3O_4 nanostructures deliver high capacity but low coulombic efficiency, which confines their practical application as anodes for LIBs. In order to obtain high Li storage capacity and eliminate the irreversible capacity at the same time, the incorporation heteroatom with the defective sites of graphene surface is found to be enable to eliminating the irreversible Li combination.It is feasible to enhance the coulombic efficiency for Fe_3O_4 nanostructures via treating the highly defective carbon component that can irreversibly consume Li ions. This strategy offers the nanocomposites with robust pathways for ion and electron transport, enabling the fabrication high performance electrodes. It is also important to mention that, spraying process is facile and scalable for industrial processes,[24-27] adapting such a scalable process allows the production of high-performance electrode materials at low cost.

Herein, we present the rational design and fabrication of hollow Fe_3O_4 nanostructures-based integrated N-doped gpaphene (G-Fe_3O_4-N) electrodes by a

facile template free hydrothermal approach combined with post-annealing.The investigation of the correlation between the detailed nanostructure of the G-Fe_3O_4-N composites and their electrochemical performance were systematically studied. The final hollow Fe_3O_4 nanostructures possess highly mesoporous texture and thin thickness, which are favorable for the fast electrochemical processes and at the same time could effectively accommodate the volume change during cycling. The citric acid serving as the reducer of GO was converted into thin carbon coating layer on the surface of Fe_3O_4 and solidifies the interface between the Fe_3O_4 and GN matrix which is beneficial to the kinetics transport of electrons and lithium ion.Such structure supplies shortened solid-phase ion diffusion length and excellent conductivity within the particles. With the further modification of GN, the electrode exhibits excellent improvements in electrochemical properties due to its large network nanostructure and high conductivity. Benefitting from the hierarchical porous texture constructed by interconnected Fe_3O_4 nanostructures as well as the smart integrated GN architectures, this integrated material can be envisioned to display high reversible capacity, enhanced cycling stability and excellent rate capability, indicating their potential application in high-performance LIBs.

Experimental

Synthesis of graphene oxide

All reagents used in the experiment were kept original and used without further purification. Graphene oxide dispersion (10 mg mL^{-1}) was firstly synthesized as per modified Hummers and Offeman's method.[28] In a typical preparation procedure, 1 g

of graphite powder (Sigma Aldrich, 5-20 mm), 1 g of NaCl, and 20 mL of H_2SO_4 were stirred together under an ice water bath condition. Subsequently, 2 g of $KMnO_4$ was slowly added into the solution. Then, the mixed solution was rapidly transferred to a 45 °C water bath and kept stirred for 2 h until a thick paste was observed, Following by the addition 80mL of water, as-prepared solution at an elevated temperature 95 °C was continuously stirred for about 1h. Then, 2.4 mL H_2O_2 was added, the color of the solution were observed from brown to yellow. The obtained warm solution was then filtered and washed with DI water for several times. The filter cake was then dispersed in water by mechanical agitation. With centrifugations at low-speed centrifugation (500 rpm) and high-speed steps 10000 rpm alternately, the final GO product is obtained .

Synthesis of G-Fe_3O_4-N

In the preparation of G-Fe_3O_4-N,2 mmol of $FeCl_3.7H_2O$ and 6 mmol of sulfosalicyclic acid sodium were dissolved in 40 mL of deionized water under stirring, citric acid (0.20g) was then added into the aqueous solution, and sodium acetate was subsequently added in order to form a stable complex solution (pH = 9.83).The synthesis procedure of pure Fe_3O_4 was the same as G-Fe_3O_4-N ,but without the addition of citric acid and GO. Then, 16 mg urea ($CO(NH_2)_2$) was added into 10 mL GO aqueous solution; subsequently, the GO mixture was added into the as-synthesized solution sealed in a Teflon lined stainless steel autoclave with a pressure of 200 MPa and maintained at 200°C for 12h.After the reaction completed, the black solid product was collected by centrifugation and washed several times with

distilled water and anhydrous ethanol. The product was dried under vacuum at 80 °C for 12 h. Finally, the collected composites were calcined at 700 °C for 10 h in a tubular furnace under N_2 at ambient conditions to gain the hierarchical hollow G–Fe_3O_4–N composite（Scheme 1）.

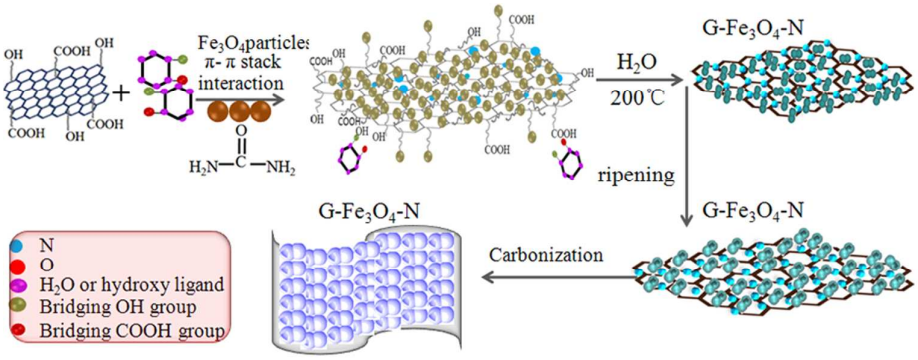

Scheme 1. Schematic illustration of the synthesis procedure of G-Fe_3O_4-N nanostructures.

Material characterization

The structures of the material were evaluated by X-ray power diffraction (XRD) on a Rigaku D/Max-2550V diffractometer using Cu Ka radiation. The morphology, microstructure and compositions of all samples were characterized by scanning electron microscopy (SEM, S-4700, Hitachi) and transmission electron microscopy (TEM, JEM-3010, JEOL).Laser micro-Raman spectrometry (RenishawinVia) and photoelectron spectroscopy (XPS, ESCALab250). Raman spectroscopy was carried out on a DXR Raman Microscope with a 532 nm excitation wavelength. Thermal gravimetric analysis (TGA) was performed in air with a heating rate of 10 °C min^{-1}.The specific surface area was evaluated by Brunauer–Emmett–Teller (BET) method at 77 K in N_2 atmosphere using Micromeritics ASAP 2010 surface area analyzer.

Electrochemical evaluation

The evaluation of electrochemical performance was conducted by means of coin-type LIBs cells (2025) assembled in an argon-filled glove box. The active materials (G-Fe_3O_4-N,G-Fe_3O_4,pure Fe_3O_4), acetylene black (conductive agent) and polyvinylidene uoride (PVDF as binder) with a mass ratio of 80: 10:10 were dissolved in N-methylpyrrolidone (NMP) to form a slurry for working electrode.The slurry was then coated onto copper foil and heated in a vacuum oven at 100 °C for 12 h.Coin cells were fabricated with working electrode, lithium metal as the counter electrode, Celgard 2400 as the separator, and $LiPF_6$ (1M) as the electrolyte in ethylene carbonate/dimethyl carbonate/diethyl carbonate (EC/DMC/DEC, 1:1:1vol%). The cell was assembled in an Ar-filled glove box. The coin cells were firstly activated at a current density of 50 mA g^{-1}, and then cycled at different current densities within the voltage range of 0.01–3.00V using a LAND-CT 2001 battery test system (Jinnuo Wuhan Corp., China).Electrochemical impedance spectroscopy (EIS) measurements were carried out via an electrochemical workstation (CHI 660 D, CHI Company) at a frequency range of 0.1 Hz to 100 kHz.

Results and discussions

Fig.1a presents the XRD pattern of Fe_3O_4 samples which can be unambiguously indexed to the pure face-centered cubic structural ($Fd\bar{3}m$ space group) magnetite Fe_3O_4 (lattice constant a= 8.3872 Å ,JCPDS card no.75-1610),which is consistent with the previously reported results. The peaks located at 18.27, 30.1, 35.42, 43.05,53.4, 56.95, and 62.52° in Fig.1a were ascribed to the (111),(220), (311), (222),

(400), (422), (511), and (440) peaks of the Fe_3O_4 composite, respectively. Compared with the pristine Fe_3O_4 particles, the peaks of G-Fe_3O_4 and G-Fe_3O_4-N are broaden, implies the formation of smaller size particles. It is noticeable that the addition of graphene prohibits the crystal growth of Fe_3O_4 particles.

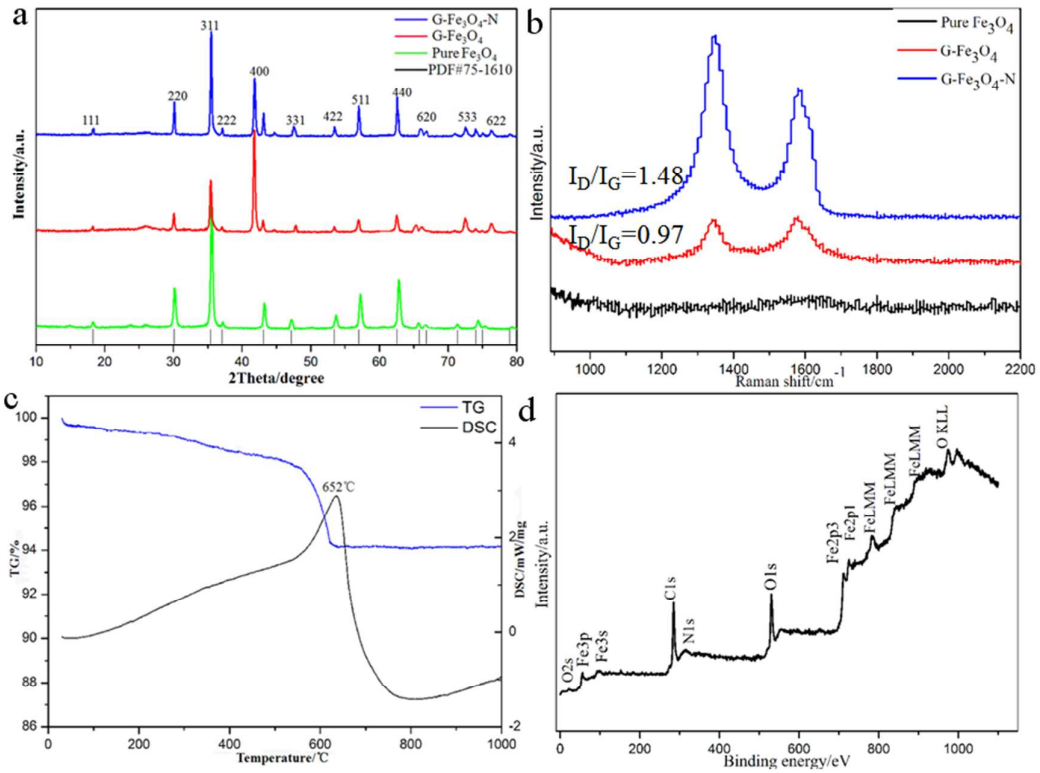

Fig.1.(a) XRD patterns of the pristine Fe_3O_4, G-Fe_3O_4;(b) Raman spectra of the Fe_3O_4 composites, the pristine Fe_3O_4, G-Fe_3O_4 and G-Fe_3O_4-N composites (c) TGA curves of the G-Fe_3O_4-N composites under oxygen flow; (d) XPS survey spectrum of G-Fe_3O_4-N at 700 °C in NH_3 atmosphere for 1 h.

Raman spectroscopy is collected for certifying the doping effect of graphene and nitrogen. intensity ratio of the D band (~1348 cm^{-1}) and G band (~1586 cm^{-1}), I_D/I_G, is the evaluation parameters of the relative concentration of local defects or disorders (especially for the sp^3-hybridized defects) compared with the sp^2-hybridized GN domains (Fig.1b).The I_D/I_G ratio for G-Fe_3O_4 and G-Fe_3O_4-N is 0.97 and 1.48,respectively.The higher defect degree for G-Fe_3O_4-N is due to the improvement

of the decomposition of citric acid and carbonization progress, more importantly, attributed to the disordered GN graphene which are usually generated intrinsically together with the nitrogen doping technique. The defects can supply extra active sites during the lithium insertion/extraction progress, which is beneficial for the electrochemical performance. Additionally, it can be concluded from the intensity and location of 2D peak for G-Fe_3O_4-N that the number of GN layers in the nanocomposite is not single or bistratal but multilayer, which is further evidenced the SEM and TEM image.

Based on the plot of thermogravimetric analysis (TGA),the content of Fe_3O_4 in G-Fe_3O_4-N hybrids is determined to be 93.8% (Fig.1c).The weight losses of G-Fe_3O_4-N was investigated by the TGA measurement from 20 °C to 1000 °C in air. The weight loss from 400 °C to 660 °C is due to the burning of GN in air, which agrees well with the prominent peak of DSC file.

To further confirm the composition and surface oxidation state of the as-fabricated Fe_3O_4 composites, X-ray photoelectron spectroscopy (XPS) identifications were also carried out. The XPS spectrum indicated the presence of N, Fe, C and O elements in the composites, identifying the successful synthesis of pure G-Fe_3O_4-N without any impurities. The deconvoluted XPS peaks of C1s centered at the binding energies of 287.7, 285.4, and 284.6eV were attributed to the C=O, C–N, and C–C, respectively (Fig.2a).[29] It can be also previously drawn that most carbon atoms were sp^2 hybridized. The two symmetric peaks at 533.5 and 529.2eV in the spectrum of O1s peak can be ascribed to the C-O and the Fe-O bond, respectively (Fig.2b). The signal of N1s is

week, indicting N predominantly existing amorphously in the composition of G-Fe_3O_4-N (Fig.2c).This confirms that GO should be reduced to N-graphene with a little amount of residual oxygen-containing group after hydrothermal reaction. The presence of metal-N bond and C-N bond in the as–prepared G-Fe_3O_4-N can be expected to supply excellent electrochemical performance. Therefore, the nitrogen atoms were also successfully introduced into the graphene nanosheets during the reduction, which derived from the urea precursor. In the Fe 2p spectrum (Fig.2d), the of $Fe2p_{3/2}$ and Fe $2p_{1/2}$, located at 710.9 and 724.5eV respectively, are attributed to the magnetite phase. The appearance of the satellite peak located at about 718.5eV certifies the formation of Fe_3O_4 instead of Fe_2O_3 in the GN matrix (Fid.2d).The XPS result is in good agreement with the following EDS spectroscopy.

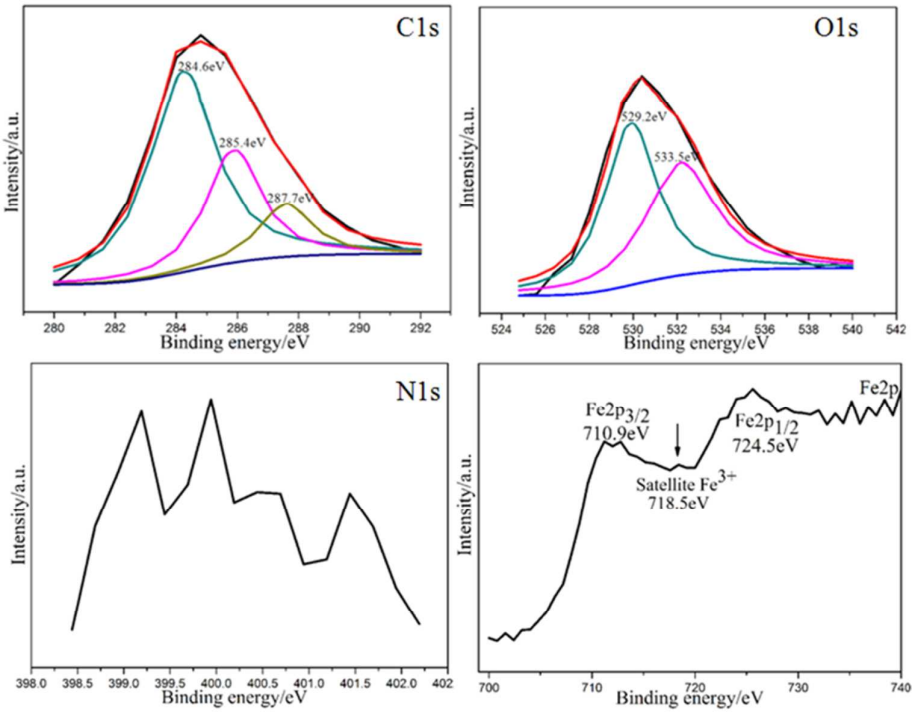

Fig.2. XPS spectrum of G-Fe_3O_4-N at 700 °C in NH_3 atmosphere for 1 h:C1s narrow scan (a) C1s narrow scan ;(b) O1s narrow scan ;(c)N1s narrow scan and (d) Fe_{2p}

narrow scan.

Fig.3a shows that the SEM image of the solid sphere-like Fe_3O_4 nanostructures with diameters of 40–50 nm. The relatively high-magnification SEM image is displayed in Fig.3b.The sample presents a serious aggregation tendency in patterns of closely packed nanoparticles which is detrimental to the penetration for electrolyte and the contact in electrode-electrolyte surface. While the G-Fe_3O_4-N nanocrystals nanocrystals are composed of tiny nanoparticles homogeneously embeded in GN building blocks with negligible aggregation phenomenon (Fig.3c and d), which is beneficial to increasing the contact surface of electrode –electrolyte. Obviously, GN prevents the growth and aggregation tendency of Fe_3O_4 nanocrystals. The hollow texture of such nanostructure is further confirmed by corresponding TEM image (Fig.4g and h), which exhibits a large void space and a well defined thin peanut like shell. In addition, the carbon layer originated from the decomposition of citric acid serves as a adhesion for connecting Fe_3O_4 and GN confining them in a intimate contact, which is beneficial for the rapid ion diffusion and electron transfer. Besides, the coating reinforces the robustness and surface hardness of the interconnected and hollow nanostructure while preserving high flexibility due to the flexible GN nanosheet and elastic hollow Fe_3O_4 feature which is exceptionally desirable during expansion of G-Fe_3O_4-N during the insertion/deinsertion of Li. Such advantages in structure can effectively alleviate the volume expansion of Li and maintain high structural integrity during the repeated cycling processes.

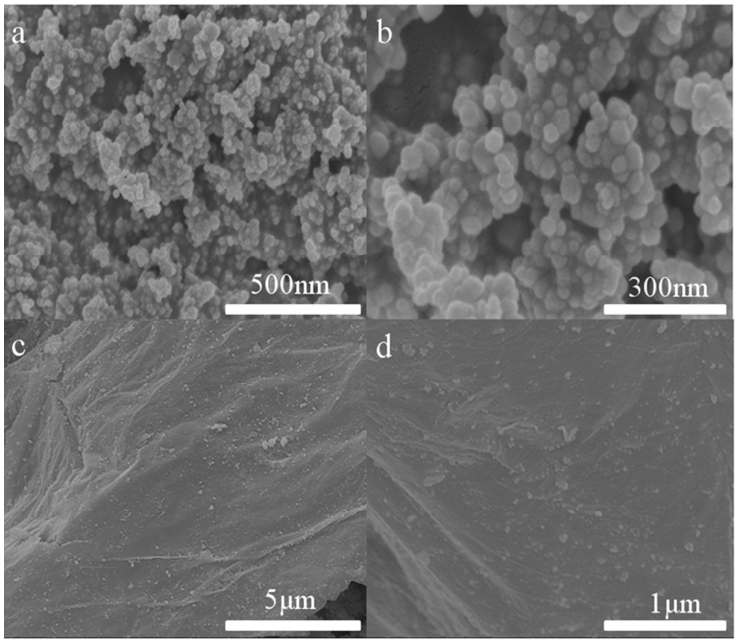

Fig.3.(a) and (b) SEM images of the pristine Fe_3O_4 sample at various magnifications;(c) and (d) G-Fe_3O_4-N composite at various magnifications.

The detailed morphological and structural features of the Fe_3O_4 are also analyzed by TEM. Fig.4a certifies the densely packed pure Fe_3O_4 sphere-like nanoparticles, which is consistent with the result of SEM image.Fig.4b shows unique HRTEM image of the Fe_3O_4, well-defined lattice fringes are clearly visible across the entire nanocrystals, with an interplanar distances of 0.485 nm and 0.297nm ascribed to the (111) and 220 d spacing of the cubic Fe_3O_4 structure, respectively. The typical FFT of the adjacent lattice planes of (220), (111) and (311) is observed from the hexagonal alinement (Fig.4c). The selected area electron diffraction (SAED) (Fig.4d) verifies that the Fe_3O_4 sample shows apparently poly- crystalline characteristic. The marked d-spacing values of the lattice planes of the core are 0.485 nm,0.297nm,0.251nm,0.242nm,and 0.210nm, which correspond well with those of (111), (220),(311), (222) and (400) planes of the Fe_3O_4 crystals, respectively. The G-Fe_3O_4-N nanocrystals of ~10nm are uniformly anchored onto the multi-layer GN

nanosheets (Fig.4e and f),which agrees well with the Raman analyses. Particularly, it should be pointed out that these nanocrystals are not agglomerated at all and present a discrete dispersion structure.It is further confirms that the incorporation of GN decreases the size and improves the uniformity of the Fe_3O_4 nanoparticles. Besides, the G-Fe_3O_4-N composites is comparatively homogeneous with the GN substrate without encapsulation of Fe_3O_4 nanostructures scarcely observed in this work.

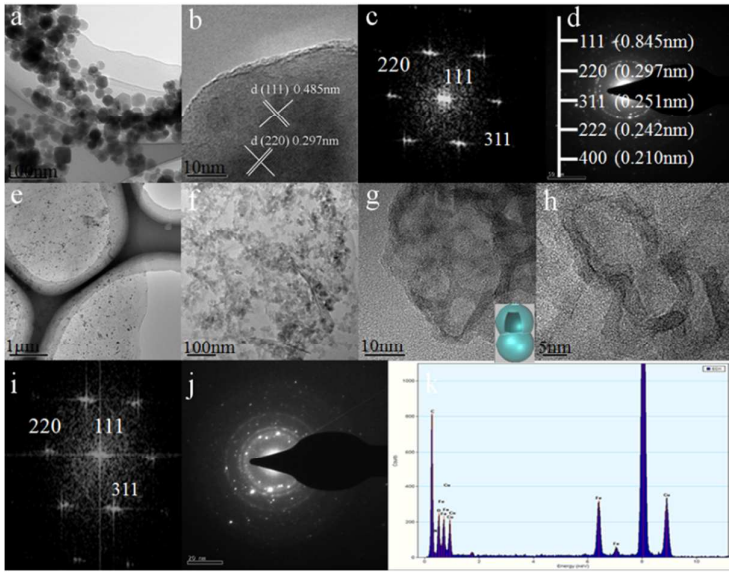

Fig.4. (a) TEM image, (b) HRTEM image, (c) FFT pattern and (d) elected area electron diffraction (SAED) pattern for pristine Fe_3O_4; (e) and (f) TEM image at different magnifications, (g) and (h) HRTEM images at different magnifications, (i) FFT pattern (j)SAED pattern and (k) element mapping for G-Fe_3O_4-N .

Fig.4g and h show the corresponding TEM image of an interesting integrated hollow peanut-shaped structure, confirming the each twinned sphere with a diameter of around 10 mm. The FFT-ED pattern along the (220),(111) (311) zone axis of the Fe_3O_4 is also observed in the Fig.4i, while the poly-crystalline nature of the composited hollow Fe_3O_4 nanostructures is obtained in Fig.4j. Another point is that, even after a long time and strong density of sonication treatment in the preparation of the TEM sample, the G-Fe_3O_4-N nanocrystals are still intimately embedded in the

interwaved GN matrix without any damage to the whole structure, as shown in Fig.4e- h, indicating the strong interaction between Fe_3O_4 nanocrystals and GN matrix. Energy-dispersive X-ray spectroscopy (EDS) certifies that the samples contain the elements C, N, Fe and O (Fig.4k),further confirming the formation of G-Fe_3O_4-N,which agree well the XRD, Raman and XPS files. The Fe/O ratio measured by EDS analysis is close to 3:4,which complies with the theoretical value.

The formation mechanism of the hollow nanostructure was also proposed. Based on energy minimization criterion, the solid Fe_3O_4 nanoparticles incline to dissolve–recrystallize on the surface of the larger size particles under high-temperature hydrothermal conditions. Driven by minimization of total surface energy, the newly formed nanocrystals aggregate into twin nanospheres. In one hand ,the thermal decomposition of urea to generate nitrogen and water vapor creates interconnected mesopores in the twin geometry. On the other hand, the nucleation oriented aggregation-recrystallization mechanism continuously functionalized and the ostwald ripening occurred to the twin spheres at the same time. As explained by the scheme1, the twin hollow nanospheres formed and reinforced left no damage because of the relatively controlled crystal growth time (8h).The GN nanosheets serving as a surface disperse agent role drive the uniform hollow nanostructures distribution on its great surface according to the entropy decreasing criterion to achieve energy balance .

By the morphology and structure analyses, it can be expected that such hollow structure provides the continuous ion transport network yielding very short charge and discharge distance while preserving elastic to accommodate the volume variation,

meanwhile, its strong interaction synergistic effect with good mechanical flexibility of high GN matrix not only prevents the agglomeration of nanocrystals into large particles, but also promotes fast electron transport through the carbon substrate to nanocrystals as well as enhancing electronic conductivity to improve the electrochemical performance.

To further investigate the hierarchical hollow microsphere structure, nitrogen adsorption and desorption measurements were conducted to estimate the texture properties. The nitrogen adsorption and desorption isotherm and pore size distribution curve of hollow G-Fe_3O_4-N nanostructure are presented in Fig.S1.The isotherm of such nanocrystals displays an obvious hysteresis loop (Fig.S1a),indicating the mesopores feature. The Brunauer–Emmett–Teller (BET) surface area of G-Fe_3O_4-N is calculated to be 114.43 m^2g^{-1}, which is higher than that of the G-Fe_3O_4 (100.52 m^2g^{-1}) and pure Fe_3O_4 (60.35 m^2g^{-1}) due to contribution of graphene and nitrogen. The plot of pore size distribution determined by the Barrett–Joyner–Halenda (BJH) method (Fig.S1b) shows that there are two sharp peaks, a dominant peak around 9.1 nm and a broad peak at 38.6 nm. The mesopores on the hollow G-Fe_3O_4-N nanostructures can be attributed to the hollow pea-nut twinspheres, namely, the void in the hollow nanostuctures which agrees well with the XRD,SEM and TEM files and the broad peak comes from interspaces of the constituent particles. The large specific surface area and high porosity offer large electrode-electrolyte contact area and promote Li^+ diffusion.[30] Benefiting from the aforementioned advantages, the Fe_3O_4-based LIBs can be expected to exhibit outstanding capacity ability, high rate

capability, and excellent cycling stability.

Based on the potential application as an anode in LIBs, the electrochemical properties of the Fe_3O_4 samples were investigated in the voltage range of 0.01–3.00 V vs. Li/Li^+.Fig.5a demonstrates the CV curves of pure Fe_3O_4 for the first 1st, 2nd, and 5th cycles at ambient temperature at a scan rate of 0.5 mV s^{-1}.The sharp reduction peak at about 0.62 V is observed in the first cathodic scan for all Fe_3O_4 microspheres, which can be assigned to the conversion of Fe_3O_4 to Fe and the formation of amorphous Li_2O ($Fe_3O_4 + 2Li^+ + 2e^- \rightarrow Li_2(Fe_3O_4)$; $Li_2(Fe_3O_4) + 6Li^+ + 6e^- \rightarrow 3Fe^0 + 4Li_2O$) as well as the irreversible reaction with the electrolyte. In this progress, the conversion of Fe_3O_4 to Fe and the formation of amorphous Li_2O takes place as the responsible factor of the irreversible capacity during the discharge process. Meanwhile, two anodic peaks at about 1.61 and 1.83 V attributed to the reversible oxidation of Fe^0 to Fe^{2+}/Fe^{3+} were observed, which conforms well with the previous reports. In the second cycle, both cathodic and anodic peaks are positively shifted in the subsequent cycles due to polarization of the electrode during the first cycle originated from the formation of solid electrolyte interface and the reaction of lithium ions with the functional groups on the GN graphene sheets after the first cycle. In following anodic and cathodic scans from 2nd to 5th, both the peak current and the integrated area intensity were nearly overlapped, implying the polarization due to the electronic resistance of active materials and the interfacial kinetic resistance resisting intercalation/extraction were negligible afterwards.[31] The CV measurements therefore indicated good electrochemical activity and stability of the Fe_3O_4 composite particles.

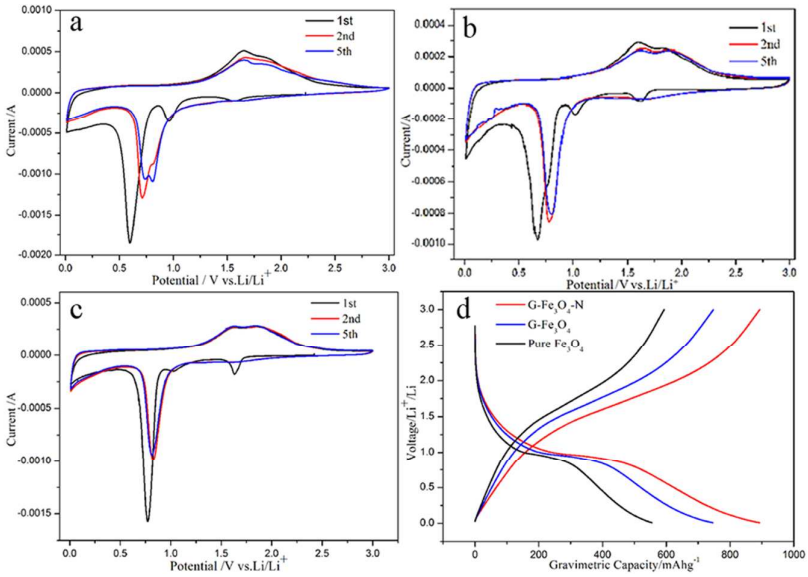

Fig.5.(a) Cyclic voltammetry curves of pure Fe_3O_4;(b) cyclic voltammetry curves for G-Fe_3O_4, and (c) cyclic voltammetry curves for G-Fe_3O_4-N at 0.5mVs^{-1};(d) initial voltage vs. capacity curves of the Fe_3O_4 samples at 50mAg^{-1}.

Compared with the pure Fe_3O_4 and G-Fe_3O_4 (Fig.5b), the current density and the integrated area of the G-Fe_3O_4-N nanocrystals (Fig.5c) are the most large due to the sufficient reaction with Li^+ of the mesoporous hollow structure, the high conductivity and the preferable pore network provided by GN sheet which is convenient for the shortened transport distance to ion and electron. It should be noted that the peak at 1.83V for the second or 5^{th} cycle of G-Fe_3O_4-N electrode, which can be ascribed to the reversible reaction to Fe_3O_4, are more obvious and intensive in patterns of much sharper and narrower peaks between anodic and cathodic peaks than that of pure Fe_3O_4 and G-Fe_3O_4,further indicating the higher reversible feature of G-Fe_3O_4-N.In one hand, the elastic hollow structure and the flexible graphene matrix can play a role as the stress buffer to relieve the volumetric stresses arising from Li ion insertion into the Fe_3O_4 particles. On the other hand, it is specially noted that such excellent reversibility is partially ascribed to the N doping (scheme 2).Irreversible Li storage is

usually caused by the irreversible lithium related to oxygen-containing functional groups (C=O,C-OH) or active carbon atoms (C^*),which promotes to the formation of SEI films on carbon surfaces.[32,33]The main products of the SEI films are Li_2CO_3, $ROCO_2Li$, etc., deriving from the irreversible combination of Li ions.Except to the pre-lithiation or Fe_3O_4 saturation of the active sites which has been confirmed to be efficient to reducing irreversible Li storage and enhancing coulombic efficiency, the selective removal of these active sites is an alternative way in this regard. According to scheme 1, the O-containing functional groups or active carbon atoms that lead to the irreversible Li storage can be been removed by the N-doping reaction owning to oxidation of NO_x or N substitution, causing a promoted reversible reaction ability ,then finally results in decreased capacity loss, in turn, an enhanced coulombic efficiency, rate performance and exceptional cycling behaviors.

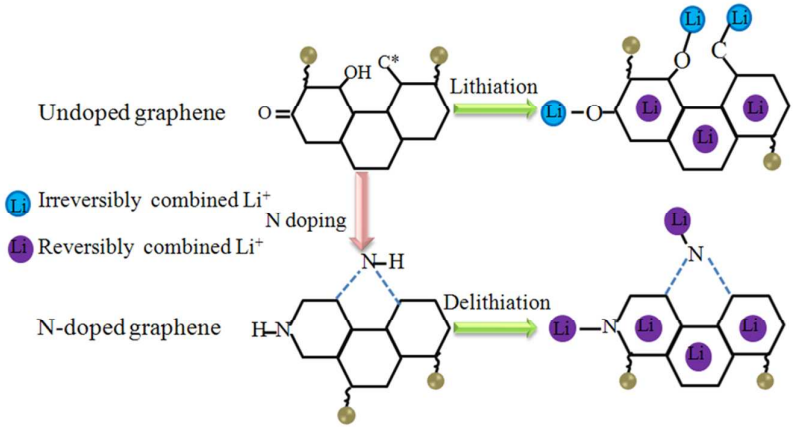

Scheme 2. Suggested mechanism for enhancing the initial Coulombic efficiency by N doping.

Constant current charging and discharging at 50 mAg^{-1} in the 0.01 to 3.00 V window was conducted next.Fig.5d depicts the charge-discharge voltage profiles of the samples at a current rate of 50$mAhg^{-1}$.It is observable that the charge/discharge

process of the three samples consists of three stages: the first stage of the quick voltage drop, the second stage of the distinct voltage plateau, and the third stage of a gradual decay in potential.Obviously,G-Fe_3O_4-N delivers a charge capacity of 895.2 $mAhg^{-1}$ and a discharge capacity of 892.1$mAhg^{-1}$,much higher than those of G-Fe_3O_4 750.8,745.7$mAhg^{-1}$ and pure Fe_3O_4 593.6,555.5 $mAhg^{-1}$,respectively.The improved electrochemical behavior is attributed to the nanosize effect, and the high conductive flexible GN matrix coupled with the hollow void space of Fe_3O_4 hollow particles that facilitates faster lithium ion insertion/deinsertion kinetics and also accommodates the volume changes taking place during the redox reactions, therefore, the charge /discharge capability of G-Fe_3O_4-N is greatly enhanced compared with pure Fe_3O_4.However,the addition of graphene should be confined in a proper amounts. The variation of charge and discharge file for G-Fe_3O_4-N as changing the contents of graphene was exhibited in Fig.S2.Compared with 3% and 5%, 4% of graphene in G-Fe_3O_4-N delivers the most excellent discharge capacity 892.1mAg^{-1} at 50$mAhg^{-1}$,higher than profile those of 4% (809.1 $mAhg^{-1}$),5% (716.4mAh g^{-1}) respectively. So once the content of graphene exceeds the threshold 4% ,the electrochemical performance of G-Fe_3O_4-N drops obviously. With too dense carbon surrounding the active Fe_3O_4,the Li ion diffusion can be blocked, therefore, 4% of graphene is the appropriate amount in this case, while the limited graphene (≤3%) could not provide enough surfaces to prohibit the agglomeration of hollow Fe_3O_4 particles, thus resulting in relatively poor electrochemical performance. Controlling Fe_3O_4 onto 4% graphene surface has significantly promoted the Li storage capacity.

It is also noticeable pointed that the addition of N improves the reversibility of lithium extraction/insertion, Li-ion diffusion and electron transport processes, bring the alleviated side reactions of the electrolyte on the electrode/electrolyte interface at high voltages, which is consistent with the CV results, and the defects and disordered surface morphology induced by N doping, offer more active sites for the lithium insertion and extraction progress, and increase electrode/electrolyte wettability, hence, having a comparison with G-Fe_3O_4, the enhanced electrochemical performance is observed for G-Fe_3O_4-N.Additionally,the hollow nanocrystals also provide a good particle/electrolyte contact area, which supply the shorter Li diffusion pathway enhancing the rate performance.

The rate performance of the Fe_3O_4 materials based electrode at different current densities from 50 to 600 mA g^{-1} are presented in Fig.6a,b and c. The corresponding discharge capacities were shown in Fig.6d.The charge–discharge capacities decrease with increase of current densities for all Fe_3O_4 nanostructured electrodes.The G-Fe_3O_4-N electrode delivers discharge capacities of 892.1, 873.5, 838.4, 804.9,and 747.5mAhg^{-1} with increasing the current density from 50 to 100, 200, 400, and 600 mAg^{-1},respectively.The G-Fe_3O_4 constructed electrode exhibits 745.7, 638.3, 715.5, 675.2, and 601.4mAhg^{-1}, while pure Fe_3O_4 composite displays 555.5,492.6,405.3,349.3, and 263.4 mAg^{-1} at 50, 100, 200, 400, and 600mAg^{-1},respectively.The enhanced charge/discharge capacity and rate capability of G-Fe_3O_4-N can certainly be ascribed to unique hollow feature with a large void space and a thin shell thickness coupled with the component composite engineering. The

mesoporous featured hollow nanostructure with thin shell domain not only provides a short Li-ion transport length because of the small particle size but also favors Li transportation kinetics. Besides, the void space and GN nanosheets effectively buffer against charge storage and the volume variations during the repeated charge–discharge process. The elastic hollow structure and GN matrix not only act as the support for Fe_3O_4 particles and provide high electrical conductivity channels , but also accommodate the volume changes and prevents the pulverization of the overall electrode during the cycling process, which concurs with the results of CV and charge/discharge. The detached pure Fe_3O_4 nanoparticles are vulnerable to aggregation during charge/discharge process, thus resulting in obvious capacity fading during electrochemical measurements.

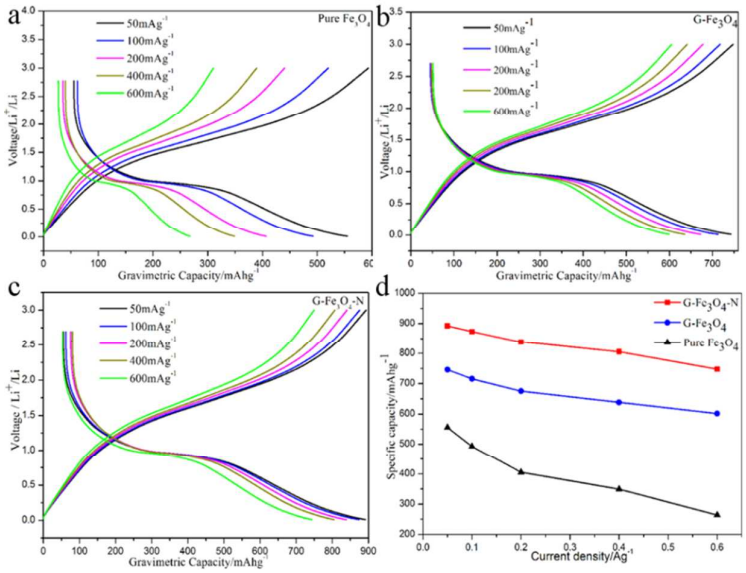

Fig.6. Charge/discharge curves of (a) pristine Fe_3O_4 sample;(b) G-Fe_3O_4 composite;(c) G-Fe_3O_4-N sample, and (d) the dependence of specific capacity on current density.

The rate and cycling performance of proof-of concept devices were further explored at various current densities from 50mA $g^{-1}$to 2000mA g^{-1}(Fig.7a).All Fe_3O_4 samples present the extra initial discharge capacity due to the formation and

decomposition of interface SEI and turn to stable in the following cycles. The G-Fe_3O_4-N delivers an average capacity of 691.5mA h g^{-1} at 800 mA g^{-1}. Even when increased to a current density as high as 2000 mA g^{-1}, a high discharge capacity of 417.6 mAh g^{-1} can still be observed. After the deep charge/ discharge for 10 cycles at 2000 mA g^{-1}, an average capacity of 417.4 mA h g^{-1} is recovered when scanned cycled at 100 mA g^{-1}. By an obvious contrast, G-Fe_3O_4 and the pure Fe_3O_4 exhibit lower capacities of 474.5 and 189.5mAh g^{-1}, respectively at 800mA g^{-1}, while much poorer rate capability 276.64 and 50.63 mAh g^{-1} at 2000 mA g^{-1} are obtained, respectively, for G-Fe_3O_4 and pure Fe_3O_4.The significantly improved lithium storage capabilities of G-Fe_3O_4-N could be probably attributed to nanosized structure, the hollow feature and the GN wrapping: (i) with a comparison to pure Fe_3O_4,the smaller size can increase contact surface with electrolyte which is beneficial to Li intercalation and de intercalation, besides the solid Fe_3O_4 particles incline to a serious aggregation tendency during charge and discharge progress which can bring capacity loss. (ii) the hollow structure can guarantee electrolyte transportation and facilitate lithium ion diffusion at the interface between the electrolyte and Fe_3O4 nanoparticles.(iii) GN can significantly enhance the electronic conductivity of the composite, creates a highly conductive network that allow efficient electron conduction among the Fe_3O_4 hollow particles via bridging adjacent Fe_3O_4 particles together.The flexible GN also reinforce the structural integrity of the active hollow nanoparticles during extended charge/discharge cycling, further improving the cyclic capacity retention of the composite.

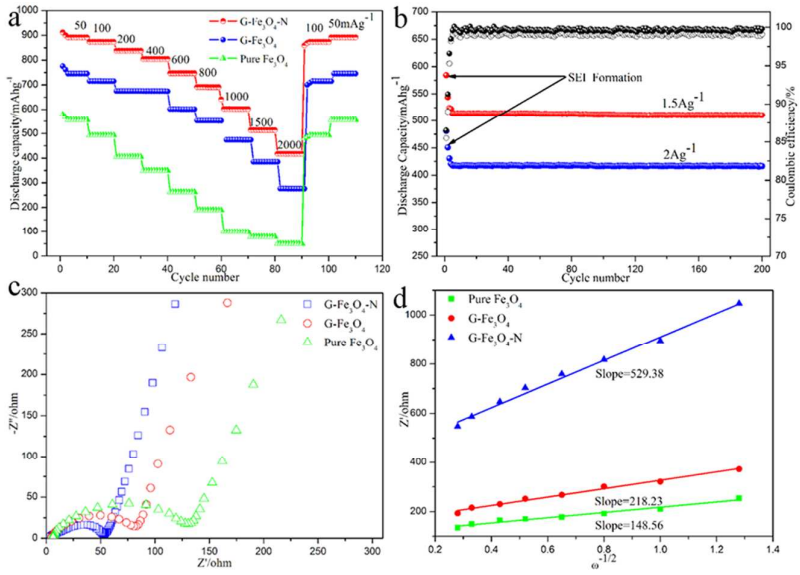

Fig.7.(a) The cycle performances of the Fe_3O_4 samples at various current rates;(b)Long-term stability for G-Fe_3O_4-N at a high current rate 1.5 A $g^{-1}$and 2 A g^{-1};(c)Electrochemical impedance spectroscopy (EIS) result of the Fe_3O_4 samples;(d) The relationship between Z_{Re} and $\omega^{-1/2}$ at low frequency.

The peanut like G-Fe_3O_4-N nanostructures also possess excellent cyclic stability at high current density.Fig.7b shows the long-term cycles versus cycle number and the corresponding coulombic efficiency at high rate .The initial reversible capacities of the nanostructures are up to 561.2 mAh g^{-1}at 1.5$Ag^{-1}$and 450.2 mAh g^{-1} at 2Ag^{-1},respectively,which declines to a value of 513.8mAh g^{-1} and 417.6mAh g^{-1}at the 3rd cycle, respectively, and then almost keep the same for the next 197 cycles at 1.5$Ag^{-1}$and 2Ag^{-1}. Besides, except to the first cycle, the coulombic efficiencies were nearly to arrive 100% at these high current densities. The excellent cycling performance of the G-Fe_3O_4-N composite is partly ascribed to a sturdy construction network from GN to accommodate and stabilize the Fe_3O_4 nanoparticles and retain the structural integrity, which efficiently prevents the aggregation of Fe_3O_4, thus maintaining the good cycling stability greatly comparable to graphene-free anodes.

The internal void space generated inside the carbon framework and hollow feature by oswald ripening process is just perfect to provide sufficient voids for the volume expansion. The surface hole supplies the convenient for active material transportation into the hollow interior, therefore, this unique structure of Fe_3O_4 has been utilized in lithium-ion batteries and presents predominant long stability. Besides, the addition of N eliminates the active sites which may bring negative reactions and increase irreversible capacity loss, which can significantly decrease the coulombic efficiency. It is obvious that the G-Fe_3O_4-N nanostructures exhibit overwhelming advantages in considering capacity, rate performance and cycling life.

To verify the stability of Fe_3O_4 hollow spherical particles, the particles were collected from coin-cells after 200cycles and investigate by TEM for any morphological changes. No pulverization, obvious aggregation or size variation were observed (Fig.S3a), and the hollow structure was well retained (Fig.S3b), indicating that such smart hollow can indeed rise the function of relieving the strain and stress caused by volume variation and preventing the agglomeration or detachment of GN sheets over cycling process. Additionally, the GN protection, prevents expansion in radial direction is obtained. Therefore, the G-Fe_3O_4-N morphology can be well-maintained during charge and discharge process. These results confirms the superior structural stability of Fe_3O_4 hollow nanostructure based electrodes.

Electrochemical impedance spectra (EIS) were carried out to understand the performance of the as-prepared Fe_3O_4 materials Fig.7c and Fig.7d.All Nyquist plots exhibit two depressed semicircles in the high-and medium-frequency regions and a

straight line in the low-frequency region (Fig.7c).The straight line in the low-frequency region is indexed to the Warburg behavior, presenting the solid-state diffusion of lithium ions into the bulk of the electrode materials. The semicircle in the medium-frequency region is attributed to the charge-transfer process. As shown in Fig.7c, there are obvious decreases of charge transfer resistance (R_{ct}) for Fe_3O_4 after the modification of graphene from 126.7 Ω to 80.3Ω and the further reduce to 51. Ω is observed after N incorporation, implies that the lithium ions and electrons can transfer more freely in the electrode/electrolyte interface in the interweaved GN frame work and the mutual interconnected hollow Fe_3O_4 nanostructures, leading to enhanced reaction kinetics and cycling stability throughout the electrode. The synergistic effect of the successful integration of the Fe_3O_4 porous structure and interweaved GN matrix is beneficial to the structure stability during charge and discharge progresses. The lithium ion diffusion coefficient in the bulk can be calculated according to the following equation:[34]

$$D=R^2T^2/2A^2n^4F^4C^2\sigma^2_W \quad (1)$$

where D is Li-ion diffusion coefficient ($cm^2\ s^{-1}$), R is gas constant (8.314 J mol^{-1} K^{-1}), T is the absolute temperature (K), A is the electrode area (cm^2), n is the number of electrons involved in the redox process (1 in our case), C is the shuttle concentration (7.69×10^{-3}mol cm^{-3}) and F is the Faraday constant (96486 C mol^{-1}).The value of σ_w is the slope of the lines between Z′ and $\omega^{-1/2}$ (Fig.7d).Clearly, the D_{Li} for G-Fe_3O_4-N is almost 4 times of that Fe_3O_4 and 2.5 times higher than that for G-Fe_3O_4. This is intensively associated with the high-quality G-Fe_3O_4-N nanocomposites can

not only alleviate the aggregation of Fe_3O_4 particles and GN nanosheets to improve the connection between active materials and electrolyte, but also offers an excellent electrical conductivity in the overall electrode. Therefore, the synergistic function of hollow Fe_3O_4 and GN together with the minimized particle size and the particular mesoporous nanostructure introduce a promising candidate for lithium storage.

Conclusions

In summary, a well developed G-Fe_3O_4-N nanostructure was successfully fabricated by a combination hydrothermal procedure and post-carbonization technology. The mesoporous peanut-like hollow nanocrystals embedded in flexible GN nanosheets delivered excellent reversible capacity, cyclic stability and high rate capability. Several factors can be attributed to unique structural and component assemble technique between Fe_3O_4 and GN, including (i) large contact areas between electrolyte and active materials for electrolyte diffusion and cushion the volume variation during the lithium-ion insertion/extraction process supplied by the hollow nanostructure.(ii) buffering of the volume variation coupled with greatly enhanced electronic conductivity provided by the uniform distribution of Graphene matrix (iii) N-doping to enhance the electrical conductivity, more beneficial active sites by the introduced defects and removal of detrimental reaction sites (iii) mesoporous structure to enhance Li ion transfer at high-rate test, and (iv) the continuous conductive network offered by the conductive GN sheets, contributing to reduction of the ion/electron transfer resistance. Particularly, structural integrity and sustained stability of the electrode guaranteed its predominant recycling ability at high current density.

Acknowledgments

The authors thankfully acknowledge the support of National Science Foundation of China (51172160).

References

1 B. Z.Jang, C. G. Liu, D. Neff, Z. N. Yu, M. C. Wang, W. Xiong, and A. Zhamu, *Nano Lett.,* 2011,**11**,3785.

2Y.G.Guo, J. S.Hu, and L. J.Wan, *Adv. Mater.,* 2008,**20**, 2878.

3J. Liu, G. Cao, Z.Yang, D. Wang, D. Dubois, X. Zhou, G. L. Graff, L. R. Pederson, and J. G. Zhang, *ChemSusChem.*, 2008,**1**,676.

4L.P.Zhu, N.C.Bing, L.L.Wang, H.Y.Jin, G.H.Liao and L.J.Wang, *Dalton Trans.*,2012,**41**, 2959.

5 E.Kang,Y. S.Jung, A. S. Cavanagh, G. H.Kim, S.M.George, A. C.Dillon, J. K. Kim, and J. Lee, Adv. Funct. Mater., 2011, **21**, 2430.

6 H.Deng, X.Li, Q.Peng, X.Wang, J.Chen, Y.Li, *Angew. Chem., Int. Ed.,* 2005,**117**, 2842.

7 H. Jiang, P. S. Lee, and C. Z. Li, *Energy Environ. Sci,* 2013, **6**, 41.

8 K.Fu, O.Yildiz, H. Bhanushali, Y. X. Wang, K. Stano, L. G. Xue, X. W. Zhang and P. D. Bradford, *Adv. Mater.,* 2013,**25**, 5109.

9 B.Koo,H.Xiong,M.D. Slater,V.B.Prakapenka, M.Balasubramanian, P. Podsiadlo, C. S. Johnson, T. Rajh , and E.V.Shevchenko, *Nano Lett.* 2012,**12**, 2429.

10M.M.Liu ,and J. Sun**,** *J.Mater.Chem.A ,* 2014,**2**, 12068.

11 X.L.Cheng, J.S. Jiang, D.M.Jiang, and Z.J. Zhao, *J .Phys .Chem. C,* 2014,**118**, 12588.

12Y.P.Gan,H.Q.Gu,H.Xiao,Y.Xia,X.Y.Tao,H.Huang,J.Du,L.S.Xu,W.K.Zhang,New.J.Chem,2014, **38**, 2428.

13Y.Wu, Y. Wei, J. P. Wang, K. L. Jiang and S. S. Fan, *Nano Lett.* 2013,**13**,818–823.

14 C.L Liang, T.Zhai,W.Wang, J.Chen, W.X. Zhao, X.H. Lu and Y.X.Tong, *J.Mater.Chem.A*, 2014,**2**,7214.

15S.Ito, K.Nakaoka, A.Kawamura, K.Ui, K.Fujimoto, and N.Koura, *J.Power Sources,* 2005,**146**,640.

16S.K. Park, S.H Yu, S. Woo, B.Quan, D.C. Lee,M.K. Kim, Y.E. Sung, and Y.Z. Piao, *Dalton Trans.,* 2013, **42**, 2399.

17Y.Q.Luo, S.S. Fan, N.Y. Hao, S.L. Zhong and W.C. Liu, *Dalton Trans.,* 2014, **43**,15317.

18 E. Kang, Y. S.Jung, A. S.Cavanagh, G. H.Kim, S. M.George, A. C.Dillon, J. K.Kim, J.Lee, *Adv. Funct. Mater.,* 2011,**21**, 2430.

19 E.J. Yoo, J. Kim, E.Hosono, H.S. Zhou, T. Kudo, I.Honma, *Nano Lett.* 2008, **8**, 2277.

20 Y.P. Liu, K. Huang, H.Luo,; H.X. Li, X.Qi, J.X.Zhong, *RSC Adv.*2014,**4** ,17653.

21 C. Ban, Z.Wu, D.T.Gillaspie, L.Chen, Y.Yan, J.L.Blackburn, and A.C.Dillon, *Adv. Mater. ,* 2010,**22**, E145.

22 L.Wang, Y. Yu, P. C. Chen, D. W. Zhang, and C.H.Chen, *J.Power Sources,* 2008,183, 717.

23 D.Deng, and J. Y. Lee, *Chem. Mat.,* 2008, **20**,1841.

24 Q. Q. Xiong, J. P. Tu, Y. Lu, J. Chen, Y. X. Yu, Y. Q. Qiao, X. L. Wang, and C. D. Gu, *J .Phys .Chem. C,* 2012,**116**, 6495.

25 P.Tartaj, and J. M. Amarilla, *J.Power Sources,* 2011, **196**,2164.
26 Z. Y.Wang, D. Y. Luan, S.Madhavi, C. M.Li, X. W. Lou, *Chem Commun.,* 2011,**47**,8061.
27 L.Li, Y.Y. Dou, L.F. Wang, M.Luo, and J.Liang, *RSC Adv,* 2014,**4** ,25658.
28 L.J. Cote, F.Kim, and J.Huang, *J. Am. Chem. Soc.,* 2009,**131**,11027.
29F.He,J.T.Fan, D.Ma, L.M. Zhang, C.Leung, and H.L.Chan, *Carbon,* 2010,**48**, 3139.
30M.Sasidharan,N.Gunawardhana, C. Senthil, M.Yoshio, and M. template, *J.Mater.Chem.A,* 2014,**2**,7337.
31 X.Y. Yao, C.L. Tang, G.X. Yuan, P. Cui, X.X. Xu, and Z.P. Liu, *Electrochem. Commun.,* 2011,**13**, 1439.
32F.Béguin, F.Chevallier, C.Vix-Guterl,S.Saadallah,V.Bertagna, J. N.Rouzaud, and E.Frackowiak, *Carbon,* 2005, **43**,2160.
33N.A.Kaskhedikar,and J.Maier, *Adv. Mater,.* 2009, **21**,2664.
34 G.H.Qin, Q.Q.Ma, and C.Wang, *Electrochim Acta,* 2014,**115**,407.